The Astrophysical Journal, 623:411–424, 2005 April 10

A STUDY OF SYNTHETIC AND OBSERVED Hα SPECTRA OF TT HYDRAE

Ján Budaj,[1] Mercedes T. Richards, and Brendan Miller
Department of Astronomy and Astrophysics, Penn State University, 525 Davey Laboratory, University Park, PA 16802;
budaj@astro.psu.edu, mtr@astro.psu.edu, bmiller@astro.psu.edu
Received 2004 November 22; accepted 2005 January 6

ABSTRACT

The formation and properties of accretion disks and circumstellar material in Algol-type systems are not very well understood. In order to study the underlying physics of these structures, we have calculated synthetic Hα spectra of TT Hya, which is an Algol-type eclipsing binary with an accretion disk. Both the primary and secondary stars were considered in the calculations, as well as a disk surrounding the primary. The Roche model for the secondary star was assumed. The synthetic spectra cover all the phases, including primary eclipse, and are compared with the observed spectra. The influence of various effects and free parameters of the disk on the emerging spectrum was studied. This enabled us to put some constraints on the geometry, temperature, density, and velocity fields within the disk. Differences found between the observed and synthetic spectra unravel the existence of a gas stream, as well as a hotter disk-gas interaction region. An additional cooler circumstellar region between the $C1$ and $C2$ Roche surfaces is suggested to account for various observed effects. A new computer code called SHELLSPEC was created for this purpose and is briefly described in this work as well. It is designed to solve simple radiative transfer along the line of sight in three-dimensional moving media. The scattered light from a central object is taken into account assuming an optically thin environment. Output intensities are then integrated through the two-dimensional projection surface of a three-dimensional object. The assumptions of the code include LTE and optional known state quantities and velocity fields in three dimensions.

Subject headings: accretion, accretion disks — binaries: close — binaries: eclipsing — novae, cataclysmic variables — radiative transfer — stars: individual (TT Hydrae)

Online material: color figure

1. INTRODUCTION

TT Hydrae (HD 97528, HIP 54807, SAO 179648, $V = 7.27$ mag, $\alpha = 11^{\rm h}13^{\rm m}$, $\delta = -26^\circ28'$) is a typical Algol-type eclipsing binary system with an orbital period of $P_{\rm orb} = 6.95$ days (Kulkarni & Abhyankar 1980) and consists of a hotter B9.5 V main-sequence primary and a cooler evolved K1 III–IV secondary star filling its Roche lobe. There is evidence of the circumstellar material in the form of an accretion disk (Plavec & Polidan 1976) surrounding the primary, as well as an indication of a gas stream (Peters & Polidan 1998). Kulkarni & Abhyankar (1980) obtained *UBV* photometric observations and photometric elements of the system. These observations were reexamined by Etzel (1988), who found from photometry, spectrophotometry, and spectroscopy $T_{\rm eff} = 9800$ K, $v \sin i = 168 \pm 5$ km s^{-1} for the primary, and $T_{\rm eff} = 4670$–4850 K for the secondary. He also suggested, on the basis of the Inglis-Teller formula, that the gas producing the UV excess and Balmer line emission has an electron number density lower than 10^{12} cm^{-3}. He also estimated a distance of 193 pc to the binary. Eaton & Henry (1992) estimated $v \sin i = 43 \pm 3$ km s^{-1} for the secondary. Plavec (1988) studied the *IUE* spectra of TT Hya and concluded from the presence of Fe II absorption lines that the vertical dimension of the accretion disk is significant and is at least comparable to the diameter of the primary. He estimated a distance to the system of 194 pc and pointed out that the presence of superionized emission lines of Si IV, C IV, and N V poses a question about the source of the ionization. Peters (1989) estimated from the eclipses of the Hα emission region that a fairly symmetrical disk fills up to 95% of the Roche lobe radius. Moreover, she argued that the disk must be rather flat, with the vertical dimension comparable to or less than the diameter of the primary. The mean electron number density in the disk was estimated to be $\sim 10^{10}$ cm^{-3}. The depth of the Hα absorption was found to be strongly variable with phase and was deepest shortly before and after primary eclipse, a feature also observed in other Algols (e.g., Richards 1993). Peters (1989) also suggested that the additional absorption in the center of the Hα line probably comes from the dense inner region of the accretion disk. She also observed that the Hα core is blueshifted relative to the primary by about 50 km s^{-1} and interpreted this as evidence of the mass outflow.

Sahade & Cesco (1946) determined the orbital parameters of the primary and identified an eccentric orbit from the Ca II H and K lines. Popper (1989) measured radial velocities of the primary and secondary and found that the motion of the secondary was consistent with the circular orbit ($K = 132$ km s^{-1}) but that of the primary was not. Van Hamme & Wilson (1993) reanalyzed the light and velocity curves separately and simultaneously and used a physical model to obtain the following parameters: separation $a = 22.63 \pm 0.12\ R_\odot$, effective temperature of the primary $T_1 = 9800$ K and secondary $T_2 = 4361$ K, radius of the primary $R_1 = 1.95\ R_\odot$ and secondary $R_2 = 5.87\ R_\odot$, mass of the primary $M_1 = 2.63\ M_\odot$ and secondary $M_2 = 0.59\ M_\odot$, and mass ratio $q = 0.2261 \pm 0.0008$. Albright & Richards (1996) obtained the first Doppler tomogram to reveal an indirect image of the accretion disk. *Hipparcos* (Perryman et al. 1997) obtained a parallax of 6.50 ± 0.95 mas. Peters & Polidan (1998) observed redshifted absorption in N I, N II lines in their far-UV spectra at the phase 0.95 and interpreted it as evidence of the gas stream and inferred the rate of inflow to be greater than $10^{-12}\ M_\odot$ yr^{-1}. Most

[1] Astronomical Institute, Tatranská Lomnica, 05960, Slovak Republic; http://www.ta3.sk/~budaj.

recently, Richards & Albright (1999) studied the Hα difference profiles and properties of the accretion region and put TT Hya into the context of other Algol binaries.

It would be interesting to verify the above estimates, conclusions, and interpretations on more physical grounds using some more sophisticated methods involving synthetic spectra that would take into account the circumstellar matter. Unfortunately, there are not many tools available for such a task at present.

There are sophisticated computer codes for calculating and inverting light curves or spectra of binary stars with various shapes or geometry including the Roche model (Lucy 1968; Wilson & Devinney 1971; Mochnacki & Doughty 1972; Rucinski 1973; Hill 1979; Zhang et al. 1986; Djurasevic 1992; Drechsel et al. 1994; Vinkó et al. 1996; Hadrava 1997; Bradstreet & Steelman 2002; Pribulla 2004). In these codes, the stars are assumed to be nontransparent and stripped of any circumstellar matter. An interesting approach for studying extended semitransparent atmospheres of some eclipsing binary components was developed by Cherepashchuk et al. (1984). Often the three-dimensional model of the circumstellar matter (behavior of state quantities and velocity field) is known or expected as a result of hydrodynamic simulations or observational constraints (see, e.g., Karetnikov et al. 1995; Richards & Ratliff 1998). Unfortunately, three-dimensional non-LTE (NLTE) calculations and spectral synthesis including complex hydrodynamics are difficult to carry out, so one alternative has been to perform a simple volume integration of emissivity, which is often too oversimplified for the particular problem.

On the other hand, highly sophisticated model atmospheres and spectrum synthesis codes have been developed assuming NLTE and plane-parallel atmospheres of hot stars (Hubeny 1988; Hubeny & Lanz 1992, 1995; Hubeny et al. 1994), spherically symmetric atmospheres (Kubát 2001), or stellar winds (Krtička & Kubát 2002). There are also sophisticated stationary plane-parallel line-blanketed model atmospheres and spectrum synthesis codes for a large variety of stars assuming LTE (Kurucz 1993a, 1993b; Smith & Dworetsky 1988; Piskunov 1992; and many others). However, these are very specialized codes and their main purpose is to calculate the spectrum emerging from a stellar atmosphere, and it is difficult to apply them to the various cases outlined above. An exception is the special case of circumstellar matter in the form of accretion disks in cataclysmic variables (CVs). In this case, the disk is approximated by a set of geometrically thin, but optically thick, static local atmospheres and the output radiation is a sum of properly Doppler-shifted local emerging intensities (Orosz & Wade 2003; Wade & Hubeny 1998; la Dous 1989). However, the case of optically thin disks or accretion disk winds, the Sobolev approximation is used (Proga et al. 2002; Long & Knigge 2002; Rybicki & Hummer 1983). Linnell & Hubeny (1996) developed a package of codes that can calculate light curves or spectra of interacting binary stars including an optically thick (nontransparent) disk. However, it is often necessary to solve the radiative transfer in a moving disk at least along the line of sight, as demonstrated by Horne & Marsh (1986). Nevertheless, their calculations assumed a linear shear and neglected stimulated emission, continuum opacity, and scattering, as well as a central star.

In this paper, we attempt to bridge the gap in the previously mentioned approaches using our new code SHELLSPEC. It is a tool that solves in LTE the simple radiative transfer along the line of sight in an optional optically thin three-dimensional moving medium. Optional transparent (or nontransparent) objects such as a spot, disk, stream, jet, shell, or stars, as well as an empty space, may be defined (or embedded) in three dimensions and their composite synthetic spectrum calculated. The stars may have the Roche geometry and known intrinsic spectra. The code is quite a multipurpose, independent, and flexible tool that can also calculate a light curve or a trailing spectrogram when necessary, or it can be used to study various objects or effects. In § 2, we describe the basic astrophysics included in the code. In § 3, we briefly mention numerical methods used in the code. In § 4.1, we study in more detail the effects of various input parameters on the spectrum of a star that has a circumstellar disk. Budaj & Richards (2004) made preliminary calculations for a single star with a disk with parameters similar to TT Hya. However, these were based on the stellar parameters found by Etzel (1988), a wedge-shape geometry of the disk with a relatively large inner radius (2.5 $R_\odot$), and no limb darkening of the primary star. More realistic stellar parameters by Van Hamme & Wilson (1993) and a slab-shaped disk geometry are used in this work. Then in § 4.2, we make more detailed calculations of the system for different phases involving both stars and a disk and compare our new synthetic spectra with real observations of TT Hya.

2. BASIC ASTROPHYSICS

This section describes the basic astrophysics included in the code. For more detailed information and a manual for the code, the reader is referred to Budaj & Richards (2004).

2.1. *Radiative Transfer*

In the following analysis, the calculations are carried out in the observer's Cartesian frame with z pointing toward the observer. The radiative transfer equation along the line of sight is

$$dI_\nu = (\epsilon_\nu - \chi_\nu I_\nu)dz, \tag{1}$$

where I_ν is the specific monochromatic intensity at the frequency ν, χ_ν is the opacity, ϵ_ν is the emissivity, and z is the distance along the beam. It is convenient to split the opacity into two contributions, the true absorption κ_ν and the scattering σ_ν:

$$\chi_\nu = \kappa_\nu + \sigma_\nu. \tag{2}$$

Assuming LTE, the line opacity corrected for a stimulated emission is stated simply as

$$\chi_\nu^{\rm line} = (1 - e^{-h\nu/kT})N_l B_{lu} h\nu\varphi_{lu}(\nu - \nu_0)(4\pi)^{-1}, \tag{3}$$

where h is Planck's constant, $h\nu$ is the energy of the transition from the lower level l to the upper level u, k is Boltzmann's constant, T is the temperature, N_l is the population of the lth state of the corresponding ion, and B_{lu} is the Einstein coefficient for the whole solid angle. The velocity field enters the equation via the shifted normalized Voigt profile $\varphi_{lu}(\nu - \nu_0)$, where

$$\nu_0 = \nu_{lu}\left[1 + \frac{v_z(z)}{c}\right], \tag{4}$$

where ν_{lu} is the laboratory frequency of the line and $v_z = \boldsymbol{v}\cdot\boldsymbol{n}$ is the radial velocity (positive toward the observer), or projection of the local velocity vector $\boldsymbol{v}$ to the line-of-sight unit vector $\boldsymbol{n}$. The Einstein coefficient, B_{lu}, is related to the oscillator strength, f_{lu}, by

$$B_{lu} = \frac{4\pi^2 e^2 f_{lu}}{m_e c h \nu_{lu}}, \tag{5}$$

where e and m_e are the electron charge and mass, respectively, and c is the speed of light. The shape of the Voigt profile is determined by the thermal and the microturbulent broadening, $v_{\rm trb}$, characterized by the Doppler half-width

$$\Delta\nu_{\rm D} = \frac{\nu}{c}\sqrt{\frac{2kT}{m} + v_{\rm trb}^2}, \tag{6}$$

as well as by the damping broadening characterized by the frame damping parameter

$$a = \frac{\gamma}{4\pi\Delta\nu_{\rm D}}, \tag{7}$$

where the damping constant

$$\gamma = \gamma_{\rm nat} + \gamma_{\rm Stark} + \gamma_{\rm VDW} \tag{8}$$

includes the contribution from the natural, Stark, and Van der Waals broadening. In the case of LTE, all the line opacity is due to the true absorption process; i.e.,

$$\kappa_\nu^{\rm line} = \chi_\nu^{\rm line}. \tag{9}$$

We also included four other continuum opacity sources: the H I bound-free opacity, the H I free-free opacity, Thomson scattering, and Rayleigh scattering on neutral hydrogen, denoted by $\kappa_\nu^{\rm H\,I\,bf}$, $\kappa_\nu^{\rm H\,I\,ff}$, $\sigma_\nu^{\rm TS}$, and $\sigma_\nu^{\rm RS}$, respectively.

The total true absorption κ_ν is the sum of the three opacity sources:

$$\kappa_\nu = \kappa_\nu^{\rm line} + \kappa_\nu^{\rm H\,I\,bf} + \kappa_\nu^{\rm H\,I\,ff}. \tag{10}$$

The total scattering σ_ν is

$$\sigma_\nu = \sigma_\nu^{\rm TS} + \sigma_\nu^{\rm RS}. \tag{11}$$

The thermal emissivity associated with the true absorption can then be written as

$$\epsilon_\nu^{\rm th} = B_\nu(T(z))\kappa_\nu, \tag{12}$$

where B_ν is the Planck function for the local value of the temperature. For scattering emissivity we have

$$\epsilon_\nu^{\rm sc} = \int\int \sigma(\nu', \nu, \boldsymbol{n}', \boldsymbol{n}) I(\nu', \boldsymbol{n}')\, d\nu'\, \frac{d\omega'}{4\pi}, \tag{13}$$

where $\sigma(\nu', \nu, \boldsymbol{n}', \boldsymbol{n})$ is the scattering coefficient containing the general redistribution function. It is this term that causes the main difficulty, since apart from redistributing the frequencies ($\nu' \rightarrow \nu$), it also couples the radiation in one direction $\boldsymbol{n}$ with the radiation field in all other directions $\boldsymbol{n}'$. However, in many applications (e.g., optically thin shells) this term can be either neglected or governed by the scattering of light from the central object. We assume coherent isotropic scattering (as seen from the scattering particle frame) from a blackbody or from a central spherical star with precalculated surface intensity I_ν^* or flux F_ν^*. In this case the emissivity reduces to

$$\epsilon_\nu^{\rm sc} = \sigma_\nu J_\nu, \tag{14}$$

where J_ν is the mean intensity. Ignoring limb darkening, J_ν can be approximated by

$$J_\nu \approx \frac{I_{\nu_1}^*\omega}{4\pi}, \tag{15}$$

where ω is the solid angle subtended by the central star and

$$\frac{\omega}{4\pi} = \frac{1}{2}\left[1 - \sqrt{1 - \left(\frac{R_*}{r}\right)^2}\right], \tag{16}$$

where R_* is the radius of the central star and r is the distance from the center (of the star/grid) and

$$\nu_1 = \nu\left(1 - \frac{v_1}{c}\right), \tag{17}$$

$$v_1 = -\frac{\boldsymbol{r}\cdot(\boldsymbol{v} - \boldsymbol{v}_*)}{r} + v_z, \tag{18}$$

where $\boldsymbol{v}$ is the velocity field vector at the given point specified by the vector $\boldsymbol{r}$ and $\boldsymbol{v}_*$ is the velocity of the center of mass of the central object.

For $R_*/r \ll 1$, an approximation including the limb darkening and the nonisotropic dipole phase function $g(\boldsymbol{n}', \boldsymbol{n}) = \frac{3}{4}[1 + (\boldsymbol{n}'\cdot\boldsymbol{n})^2]$ can be used:

$$\epsilon_\nu^{\rm sc} = \frac{3}{4}\left(1 + \frac{r_z^2}{r^2}\right)\sigma_\nu J_\nu, \tag{19}$$

where

$$J_\nu \approx \frac{F_{\nu_1}^*}{4\pi}\frac{R_*^2}{r^2}, \tag{20}$$

where

$$F_{\nu_1}^* = \pi I_{\nu_1}^*\left(1 - \frac{u}{3}\right), \tag{21}$$

where u is the limb-darkening coefficient.

The total emissivity is then

$$\epsilon_\nu = \epsilon_\nu^{\rm th} + \epsilon_\nu^{\rm sc}, \tag{22}$$

and the total source function is

$$S_\nu = \frac{\epsilon_\nu}{\chi_\nu}. \tag{23}$$

The radiative transfer equation along the line of sight is solved (see § 3), and the flux, F_ν, from the object at the Earth is then obtained by the integration of the output intensities through the two-dimensional projection surface of the three-dimensional object.

2.2. *Roche Geometry*

Both objects, star and companion, may have shapes according to the Roche model for detached or contact systems. Descriptions of the Roche model can be found in Kopal (1959), Limber (1963), Plavec & Kratochvil (1964), Mochnacki & Doughty (1972), Hilditch (2001), and many other papers and books. Most of them use cylindrical coordinates, but we assume a Cartesian coordinate system (x, y, z) centered on one of the stars (labeled as 1) such that the companion (labeled as 2) is at (1, 0, 0) and revolves around the z-axis in the direction of the positive y-axis. Let the mass ratio, q, always be m_2/m_1, or "companion/star," and $q < 1$ will indicate that the central star is heavier while $q > 1$ means the central star is lighter. We also assume synchronous rotation; i.e., the stellar surface rotates with the orbital period.

Then, the normalized Roche potential, $C(x, y, z)$, is expressed as

$$C = \frac{2}{(1+q)r_1} + \frac{2q}{(1+q)r_2} + \left(x - \frac{q}{1+q}\right)^2 + y^2, \quad (24)$$

where

$$r_1 = \sqrt{x^2 + y^2 + z^2}, \quad (25)$$

$$r_2 = \sqrt{(x-1)^2 + y^2 + z^2}. \quad (26)$$

The Roche surface of a detached component is defined as an equipotential surface $C_s = C(x_s, y_s, z_s)$ passing through the substellar point (x_s, y_s, z_s) (point on the surface of the star in between the stars, $0 < x_s < 1, y_s = z_s = 0$), which is localized by the "fill-in" parameter $f_i \leq 1$. We define this by

$$f_i = \frac{x_s}{L_{1x}}, \quad f_i = \frac{1 - x_s}{1 - L_{1x}}, \quad (27)$$

for the primary and the secondary, respectively. Here L_{1x} is the x-coordinate of the L1 point at $(L_{1x}, 0, 0)$. The Roche equipotential surface C_s of a contact system will be defined by the fill-out parameter $1 < f_o \leq 2$:

$$f_o = \frac{C1 - C_s}{C1 - C2} + 1, \quad (28)$$

where potentials $C1$ and $C2$ correspond to the potentials at the L1 and L2 points, respectively. First, we calculate L1, L2, C_s, and x-boundaries of the object using the Newton-Raphson iteration method in the x-direction, and then the three-dimensional shape of the surface is solved using the Newton-Raphson iteration in y- and z-coordinates with a precision of about 10^{-5}.

Gravity darkening is taken into account by varying the surface temperature according to the following law (Claret 1998):

$$\frac{T}{T_p} = \left(\frac{g}{g_p}\right)^{\beta}, \quad (29)$$

where g is the normalized surface gravity, β is the gravity-darkening exponent, and T_p and g_p are the temperature and gravity at the rotation pole, respectively. The normalized gravity vector is $\boldsymbol{g} = (C_x, C_y, C_z)$ and

$$g = \sqrt{C_x^2 + C_y^2 + C_z^2}, \quad (30)$$

where

$$C_x = \frac{\partial C}{\partial x}, \quad C_y = \frac{\partial C}{\partial y}, \quad C_z = \frac{\partial C}{\partial z}. \quad (31)$$

The gravity-darkening factor of the surface intensity is then calculated as

$$f_{\rm GD} = \frac{B_\nu(T)}{B_\nu(T_p)}. \quad (32)$$

Note that there is an imminent singularity in the calculations in the vicinity of the L1and L2 points, since gravity falls to zero, which drags temperatures (a denominator in many equations) to zero. We avoid the problem by setting the lowest possible value of $g/g_p = 10^{-4}$. Limb darkening is taken into account using equation (42) and by calculating the cosine of the angle θ between the line-of-sight unit vector $\boldsymbol{n} = (n_x, n_y, n_z)$ and a normal to the surface:

$$\cos\theta = -\frac{\boldsymbol{n}\cdot\boldsymbol{g}}{g} = -\frac{n_x C_x + n_y C_y + n_z C_z}{\sqrt{C_x^2 + C_y^2 + C_z^2}}. \quad (33)$$

The reflection effect is not included in the present version.

3. NUMERICAL PERFORMANCE

3.1. *Solving the Radiative Transfer Equation*

A number of optional objects (including transparent, nontransparent, and empty space) can be defined within the model, and the line of sight may cross several of them within a few grid points. A simple and stable method is needed to cope with such velocity, density, and temperature fields, which are optional and are allowed to be noncontinuous. Our problem is that of the integration of a first-order ordinary differential equation with known initial values at one boundary. The equation of the radiative transfer along the line of sight at the frequency ν is integrated with an analog of the midpoint method (Budaj & Richards 2004). It can be written in the discretized form

$$\frac{I_{i+1} - I_i}{z_{i+1} - z_i} = \epsilon_{i+1/2} - \frac{\chi_{i+1/2}(I_{i+1} + I_i)}{2} \quad (34)$$

and simply integrated via the recurrent formula

$$I_{i+1} = \frac{S_{i+1/2}}{A + 1/2} + I_i \frac{A - 1/2}{A + 1/2}, \quad (35)$$

where

$$A = \frac{1}{\chi_{i+1/2}(z_{i+1} - z_i)} \quad (36)$$

and

$$S_{i+1/2} = \frac{\epsilon_{i+1/2}}{\chi_{i+1/2}}, \quad I_1 = 0, \quad (37)$$

where

$$\epsilon_{i+1/2} = \frac{\epsilon_i + \epsilon_{i+1}}{2}, \quad \chi_{i+1/2} = \frac{\chi_i + \chi_{i+1}}{2}. \quad (38)$$

If the line of sight happens to hit a nontransparent object, the integration starts on the other side of the object with the boundary condition

$$I_1 = I^*(\nu_2) f_{\rm LD} f_{\rm GD}, \quad (39)$$

or

$$I_1 = B_{\nu_2}(T_{\rm eff}) f_{\rm LD} f_{\rm GD}, \quad (40)$$

where ν_2 is the Doppler-shifted frequency in the comoving frame corresponding to the frequency ν of the observer's frame,

$$\nu_2 = \nu\left(1 - \frac{v_z^*}{c}\right), \quad (41)$$

and v_z^* is the radial velocity of the surface of the nontransparent object where it intersects the line of sight. Here I^* is the surface intensity of the nontransparent object perpendicular to the surface in the comoving (frozen to the surface) frame. If I^* is not available, it can be calculated, e.g., using equation (21) from the known surface flux. Rotation of the nontransparent objects is

fully taken into account here by including it into the calculations of v_z^*. The quantity $f_{\rm LD}$ is a limb-darkening factor:

$$f_{\rm LD} = 1 - u + u\cos\theta, \tag{42}$$

where u is the limb-darkening coefficient and θ is the angle between the normal to the surface of the nontransparent object and the line of sight. The quantity $f_{\rm GD}$ is a gravity-darkening factor, which is important in the case of Roche geometry (see the § 2.2) and in which case $T_{\rm eff} = T_p$ is the temperature at the rotation pole of a detached star or the temperature at the rotation pole of the more massive star in the case of a contact system; otherwise, it is the common effective temperature of the spherical star. If the line of sight happens to pass through an empty space, this region is skipped and the integration continues with $I_{i+1} = I_i$.

The SHELLSPEC code enables the user to look at the object from different points of view and to calculate the corresponding spectra. The input model of the shell is defined in its "body frozen" Cartesian coordinates (x'', y'', z'') with the z'' axis corresponding to the intrinsic rotation axis of the model. The spectrum is always calculated in the observer's "line of sight" Cartesian frame [(x, y, z) with z pointing to the observer], which has the same center of coordinates.

3.2. *Additional Information and Adopted Routines*

The code assumes the known behavior of state quantities: temperature T, density ρ, and electron number density n_e. Solar abundances are assumed (Grevesse & Sauval 1998), but the user is allowed to change all the element abundances. The level populations are obtained from the Boltzmann and Saha equations. Partition functions (routine *pfdwor*) were taken from the UCLSYN code (Smith & Dworetsky 1988; Smith 1992). A FORTRAN77 code containing the partition function routines is also available in Budaj et al. (2002). The Gaunt factors (routines *gaunt* and *gfree*) and Voigt profile (routine *voigt0*) are calculated with the subroutines taken from the SYNSPEC code (Hubeny et al. 1994). If the damping constants are not known, they are estimated in the code in a way analogous to the SYNSPEC code. We also adopted the atomic data for chemical elements (routine *state0*) from SYNSPEC and routines *locate* and *hunt* from Press et al. (1986). We also used a few sections from our previous original codes for calculations of radiative accelerations in stellar atmospheres of hot stars (Budaj & Dworetsky 2002). Apart from the above, the code was written from scratch and provides an independent tool to study a large variety of objects and effects; cgs units are used within the code and the paper if not specified otherwise.

4. APPLICATION TO ACCRETION DISKS IN TT HYA TYPE SYSTEMS

4.1. *The Effects of Various Free Parameters on the Emerging Spectrum*

Before we modeled the complex spectrum of the two stars and the disk, we studied the effects of various free parameters on the spectrum. To comprehend the problem more easily we restricted our calculations to the following assumptions. We neglected the secondary and studied only the primary star surrounded by a disk. The primary was treated as a spherical blackbody with the following parameters: effective temperature $T_{\rm eff} = 9800$ K, mass $M = 2.63\ M_\odot$, radius $R = 1.95\ R_\odot$ (Van Hamme & Wilson 1993), and limb darkening $u = 0.5$. The disk was characterized by a slab of vertical half-width $\alpha = 2\ R_\odot$, which was further constrained by two spherical surfaces with the inner radius $R_{\rm in} = 2\ R_\odot$ and the outer radius $R_{\rm out} = 10\ R_\odot$. The electron number density of the disk was set to $n_e = 3\times10^9$ cm^{-3}, density $\rho = 5\times10^{-15}$ g cm^{-3}, temperature $T = 7000$ K, microturbulence $v_{\rm trb} = 0$ km s^{-1}, and inclination $i = 82\overset{\circ}{.}84$. We adopted the following velocity field $\boldsymbol{v}$ of the disk:

$$\omega(r) = \sqrt{G\frac{M}{r^3}}, \quad \boldsymbol{v} = \boldsymbol{\omega}\times\boldsymbol{r}, \tag{43}$$

where M is the mass of the central object, G is the gravitational constant, and $\boldsymbol{\omega}$ and $\boldsymbol{r}$ are the angular velocity and radius vectors, respectively. The above prescription for the velocity reduces to the well-known Keplerian velocity field in the limit of zero vertical thickness of the disk. The calculations were performed on the Cartesian three-dimensional grid with the typical resolution in the disk plane of 121×121 points. Figures 1, 2, and 3 illustrate the effects of varying just one of these free parameters of the system.

The top of Figure 1 displays the effect of increasing the vertical half-thickness of the disk from 0.5 to 5 $R_\odot$. The overall emission increases as we increase the emitting space volume, and the central absorption decreases mainly for the thicker disks. This occurs because the central depression is partly produced by the material projecting onto the star and there is more material in the Keplerian disk that does not project onto the stellar disk (surface) for thicker disks, thereby filling the central absorption. This is not true for very thin disks, as it essentially causes the disk and its line profile to diminish and both emission and central absorption approach the continuum level. Contrary to the case of the wedge-shaped disk (Budaj & Richards 2004), we observe that in a slab disk geometry the blue/red line profile wings of the thick disks ($\alpha > 3\ R_\odot$) do not change much and emission peaks get slightly closer.

The middle section of Figure 1 displays the effect of changing the outer radius of the disk from 6 to 14 $R_\odot$. The emission increases as the emission volume increases. This parameter has a strong effect on the position of the emission peaks and width of the central depression. The peaks get closer and the central depression narrower for larger radii as more matter is involved at lower Keplerian velocities. The depth of the central absorption varies very little, since the amount of the matter projected onto the stellar surface does not vary as much as in the previous case. This absorption first deepens as the overall emission becomes more pronounced and then for $R_{\rm out} > 12\ R_\odot$ weakens as the fraction of the gas projecting on the stellar disk decreases. The blue and red wings of the line are not affected at all.

The bottom part of Figure 1 displays the effect of increasing the inner radius of the disk from 2 to 8 $R_\odot$. Contrary to the outer radius, the inner radius has little effect on the emission from the beginning when it is a small fraction of the outer radius, since it does not change the emission volume noticeably. The changes are mainly seen in the far wings of the profile, since the higher Keplerian velocities are involved. It is only when it approaches the outer radius that the overall emission starts to decline and the line weakens as the emission volume decreases, and the shape of the profile acquires the new U-type shape with a central hole. This shape indicates that the central depression is created by two different mechanisms (see below).

In Figure 2 (*top left*), we inspect what happens if we vary the stellar radius from 1.5 to 3.0 $R_\odot$. The stellar radius certainly affects the amount of matter projected onto the stellar surface, but it also raises the continuum level and dilutes the emission from the disk. This is the main reason why the emission weakens for bigger stars. At the same time, the central absorption gets

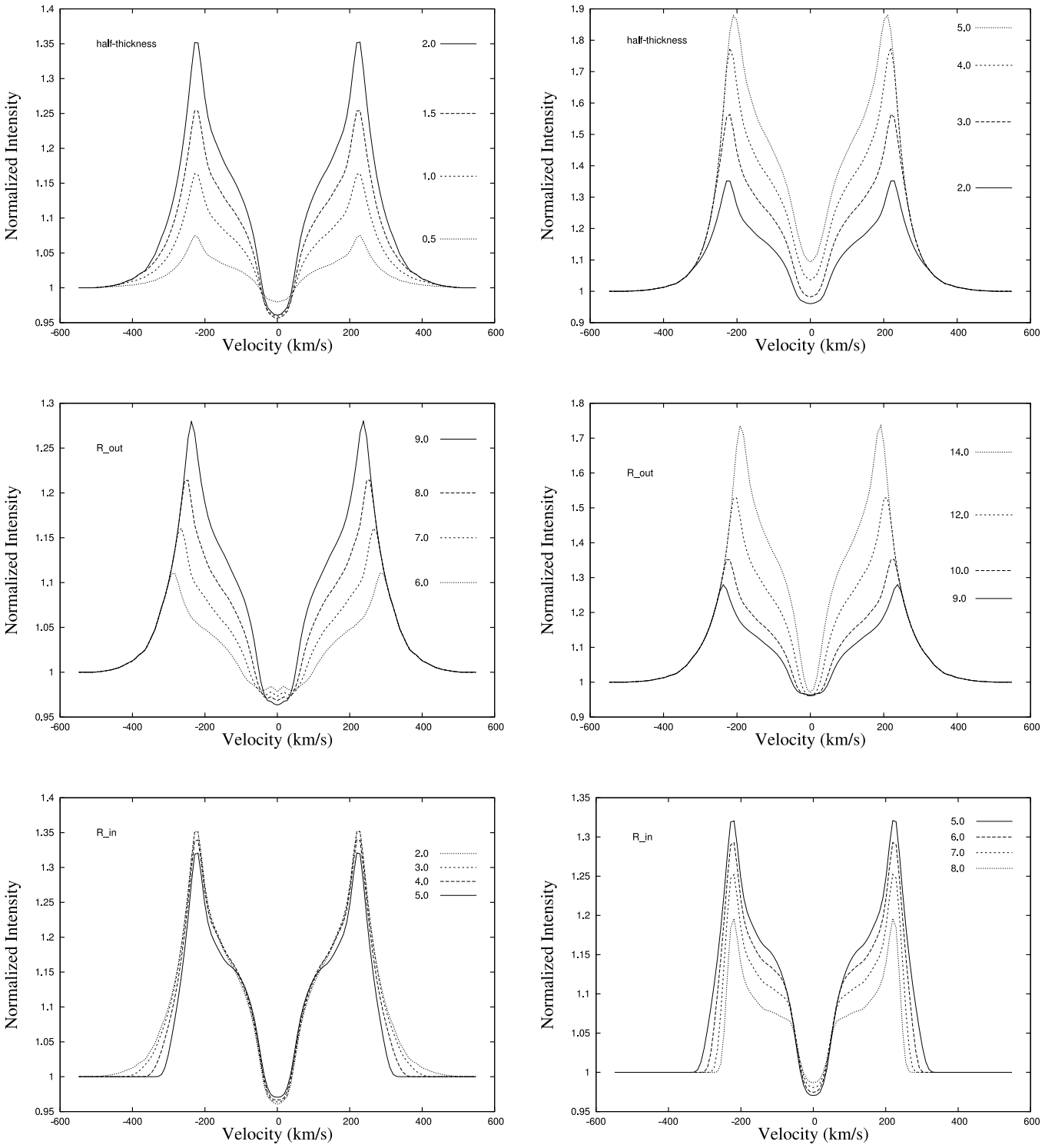

FIG. 1.—*Top left:* Effect of varying α (vertical half-width of the disk) from 0.5 to 2 $R_\odot$; *top right:* effect of varying vertical half-width of the disk from 2 to 5 $R_\odot$; *middle left:* effect of varying the outer radius of the disk from 6 to 9 $R_\odot$; *middle right:* effect of varying the outer radius of the disk from 9 to 14 $R_\odot$; *bottom left:* effect of varying the inner radius of the disk from 2 to 5 $R_\odot$; *bottom right:* effect of varying the inner radius of the disk from 5 to 8 $R_\odot$.

wider because the matter projected onto the stellar disk spans a broader radial velocity interval. When varying the stellar radius, it may happen that the star overlaps the inner radius of the disk. In such a case, the program sets both radii to be equal.

We also illustrate here the line profiles if the disk were viewed from different inclination angles (Fig. 2, *top right*). Starting from edge-on, $i = 90^\circ$, the two emission peaks have the lowest intensity, and we also observe the largest separation of the emission peaks and the deepest central depression. This is where we encounter the highest radial velocities and also where most of the disk projects onto the stellar surface. As the inclination decreases and we begin to see the disk pole-on, the emission peaks increase and their separation and central depression vanish, eventually merging into single-peak emission for $i = 0^\circ$. One can also see that the central depression is caused by two different effects. The velocity field and geometry of the disk itself can

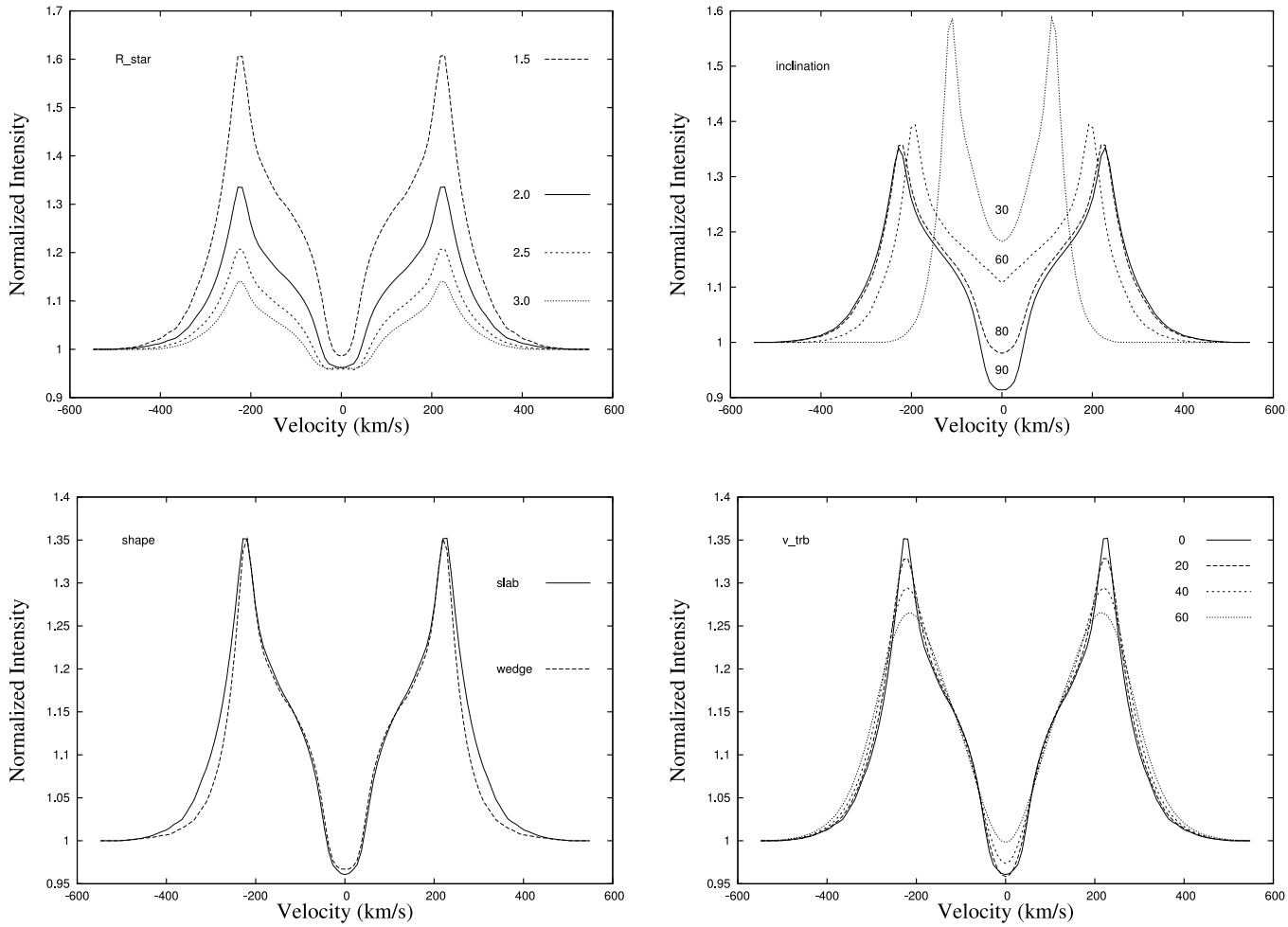

FIG. 2.—*Top left:* Effect of varying the radius of the star from 1.5 to 3.0 $R_\odot$; *top right:* effect of changing the inclination of the disk from 90° to 30°; *bottom left:* effect of the geometrical shape of the disk; *bottom right:* effect of increasing the microturbulence in the disk from 0 to 60 km s^{-1}.

produce the U or V type of depression. Superposed on that is the absorption by the cool matter projected onto the hotter stellar surface, which quickly diminishes if viewed out of the disk plane.

It is interesting to explore how the shape of the profile changes if the geometry of the disk changes. The prescription for the velocity field remains the same. In Figure 2 (*bottom left*), we compare two profiles: One is obtained for the slab-shaped disk with the standard parameters listed above. The other disk has the shape of a rotating wedge with the wedge angle $\alpha = 28°$, which produces emissions of similar strength to the slab disk model. All other parameters were the same. It is clear that the main difference is in the wings, which are more pronounced in the slab model, since there is more matter closer to the star in that model than in the wedge model.

Apart from the state quantities and velocity field, every space point can be assigned a value of microturbulence. It is included in the calculation of thermal broadening as an additional thermal motion and can thus be used to model chaotic velocity fields on a scale smaller than the mean free path of a photon. It turns to be a useful free parameter, since the mass transfer may not be a smooth process and the velocity field of the spiraling gas in the disk may well depart from the circular Keplerian orbits and be turbulent, and these departures may easily exceed the sound velocity, which is of the order of 10 km s^{-1}. Figure 2 (*bottom right*) illustrates the effect of increasing the microturbulence in the disk from 0 to 60 km s^{-1}. Note that the inner radius Keplerian disk velocity is about 500 km s^{-1}. The emission peaks are gradually smoothed and are broader. The behavior of the central absorption is more complicated and interesting. From the beginning it gets narrower and even deeper because of the desaturation effects of the microturbulence, but then the smoothing effect prevails. The microturbulence affects the optical depth along the line of sight. While the surface of the star is seen at an optical depth of approximately 1.5 (at the frequency of the line center) without the microturbulence, it is seen at optical depths of 0.7 and 0.4 for microturbulence of 20 and 40 km s^{-1}, respectively. Without the turbulence and assuming the input parameters mentioned above, the line opacity was found to be about 3 orders of magnitude higher than the continuum opacity in the line center. Thomson scattering was the most important continuum opacity source and was a factor of 300 higher than the hydrogen bound-free contribution, while H bound-free opacity was a factor of 20 higher than the hydrogen free-free opacity, and H free-free opacity a factor of 30 higher than Rayleigh scattering opacity in the disk. This pattern, however, will be very sensitive to the state quantities, wavelength, and line absorption coefficient.

Figure 3 (*top left*) displays the effect of increasing the electron number density of the disk from 1×10^9 to 5×10^9 cm^{-3}. Here we assume that hydrogen is almost fully ionized, in which case the density is linearly proportional to the electron number density. This strongly enhances the emission peaks and slightly deepens the central absorption. This huge impact on the emission can be understood, since the equivalent width in the optically thin case is

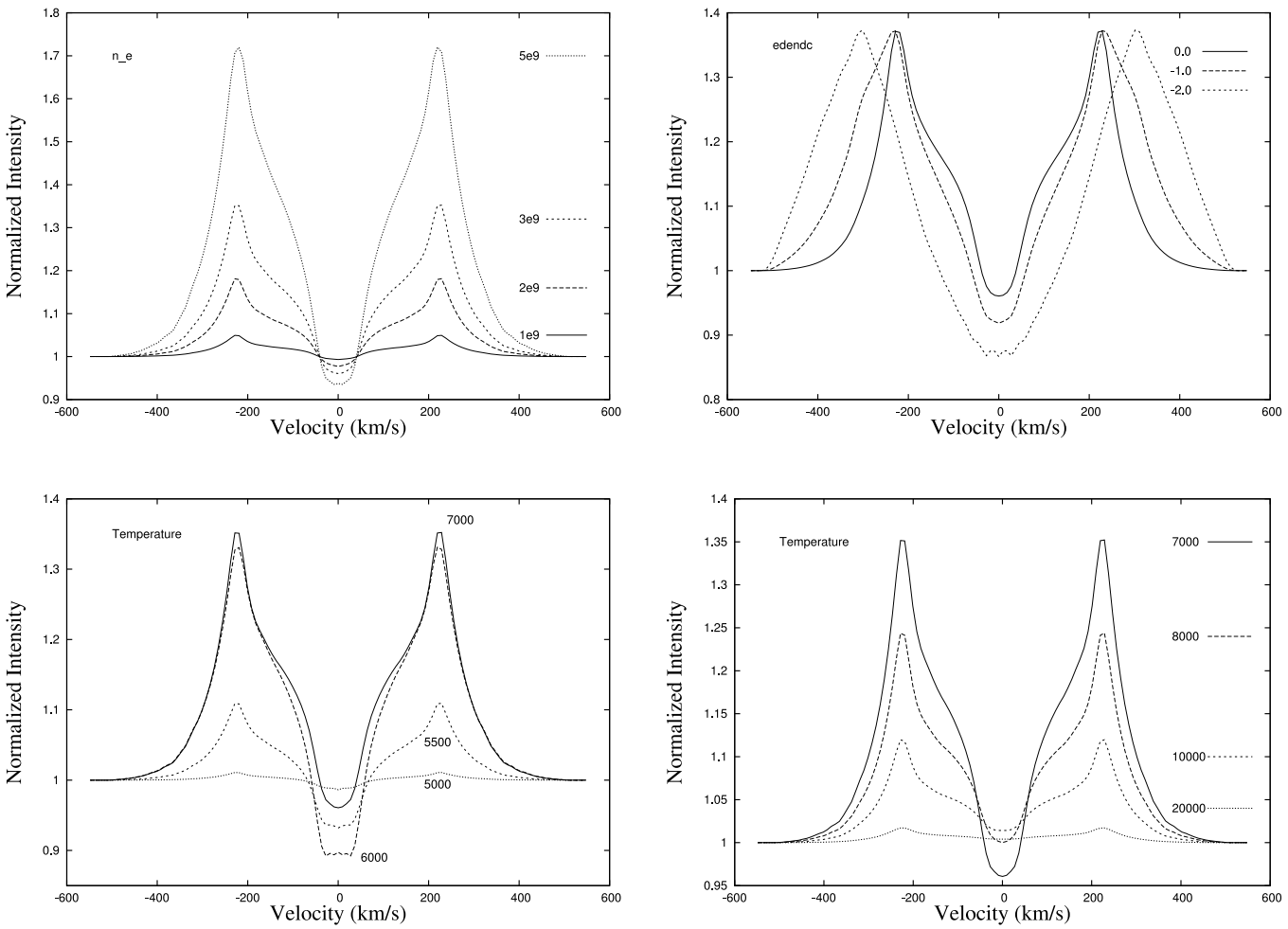

FIG. 3.—*Top left:* Effect of varying the density and the electron number density of the disk; n_e varies from 1×10^9 to 5×10^9 cm^{-3}, $\rho \sim n_e$; *top right:* effect of varying the exponent η of the power-law behavior of the densities $\rho \sim r^{\eta}$ in the disk from 0 to -2; *bottom left:* effect of varying temperature of the disk from 5000 to 7000 K; *bottom right:* effect of varying temperature of the disk from 7000 to 20,000 K.

proportional to the population of the particular level, which in turn is proportional to the total H I population. However, the ionization fraction of neutral hydrogen is proportional to the electron number density, and if the latter is also proportional to the density, it follows that the total H I population increases with the square of the density or the electron number density assuming the hydrogen abundance and temperature are fixed ($n_{\rm H\,I}/n_{\rm H\,II} \approx n_{\rm H\,I}/n_{\rm H} \sim n_{\rm H\,I}/\rho \sim n_e \sim \rho$). As a consequence, the equivalent width, EQW, should also behave like $\sim n_{\rm H\,I} \sim \rho^2 \sim n_e^2$, which is seen in Figure 3.

Since the emission is so sensitive to the density, we also studied the effect of different density profiles (Fig. 3, *top right*). Let the density and electron number density be inhomogeneous and have a power-law dependence on the distance from the star, namely, $\rho \sim r^{\eta}$. This was achieved by varying the exponent *edendc* $\equiv \eta$ from 0.0 to -2.0 and by normalizing the synthetic spectrum to the same emission peak strength. It is apparent from the figure that the line profiles for lower exponents are broader and have steeper wings while those for higher exponents have a narrower and smaller central depression. This can easily be explained, since the lower exponents emphasize the matter close to the star with higher Keplerian velocity while the opposite is true for the higher exponents. Contrary to what was found by Budaj & Richards (2004) for a wedge-shaped disk with an inner radius of 2.5 $R_\odot$, the position of the emission peaks in a slab disk model with $R_{\rm in} = 2\ R_\odot$ is much more sensitive to this exponent.

Figure 3 (*bottom left and bottom right*) also displays the effect of varying the temperature of the disk over the interval 5000–20,000 K. The emission is strongest at about 7000 K and declines toward higher temperatures as the fraction of neutral hydrogen declines because of ionization. The emission also declines toward cooler temperatures as it decreases the population of the lower level from which the Hα originates. At the same time, the temperature of the disk has a strong effect on the depth of the central absorption, which grows toward the cooler temperatures. For temperatures $T < T_{\rm eff}$, the line source function along the line of sight hitting the stellar surface steps down from the stellar surface to disk and toward the observer. For higher temperatures $T > T_{\rm eff}$, this component of the source function steps up, reducing the central depression. For temperatures both cooler and hotter than 7000 K, the line-to-continuum emissivity decreases (the continuum is provided mainly by the star and is essentially constant) and the line disappears from the spectrum, forcing the central depression to merge with continuum as well. This is the reason why the central depression also ceases below 6000 K, even though the line source function steps down. The cooler disks, if they were denser, could produce even deeper central absorption. Nevertheless, one can see that disks or regions with temperatures below 5000 K or above 30,000 K are

not capable of producing strong Balmer line emissions and that most such emissions observed in the Algols or CVs must originate from the aforementioned temperature regions.

We would like to emphasize that these calculations do not aim to calculate the physical model of the disk. The model is assumed to be known. The previous calculations illustrate the effect of varying just one free parameter at a time while keeping all the others fixed. In many cases this may not represent the real behavior of the system, since some quantities may be more or less interlocked, such as temperatures and electron number densities.

4.2. *Modeling of the Observed Spectra of TT Hya*

Now that we understand the influence of various parameters on the emerging spectrum, we can proceed to fit the complex spectrum of TT Hya. We used 23 observed spectra from 1994 of Richards & Albright (1999), complemented by 24 new spectra from 1996/1997. A detailed study of these spectra will be published in B. Miller et al. (2005, in preparation) and will include the actual measurements of the intensity of the central depression and the emission peaks.

We performed some new and more sophisticated calculations of synthetic spectra in which both stars and a disk were considered. The primary was treated as a rotating solid sphere, while the surface of the secondary was modeled in terms of the Roche model. The stellar properties were based on the absolute parameters of the system obtained by Van Hamme & Wilson (1993) and are summarized in Table 1. Since our code accepts the polar temperature, T_p, for the Roche model rather than the average surface temperature, we adopted the value $T_p = 4600$ K, which is slightly higher than the average temperature $T = 4361$ K obtained by Van Hamme & Wilson. Their V-band limb-darkening coefficients were adopted here. Values for the surface gravity of $\log g = 4.23$ for the primary and $\log g = 2.66$ for the secondary were assumed. First, we obtained the model atmospheres of both stars by interpolating in the Kurucz (1993b) $T_{\rm eff}-\log g$ grid and assuming solar abundances and a microturbulence of 2 km s^{-1}. Next, we calculated the intrinsic synthetic spectra emerging from these atmospheric models (flux from the unit area of the surface) using the code SYNSPEC (Hubeny et al. 1994) modified by Krtička (1998). Here again, solar abundances and a microturbulence of 2 km s^{-1} were assumed. These synthetic intrinsic spectra were then assigned to the primary and secondary for the calculation of the complex spectra of both stars and the disk using SHELLSPEC. On the basis of the lessons learned in the previous section, we manipulated the free parameters of the disk so that the observed spectra could be reproduced. We assumed that the electron number density is equal to the hydrogen number density. A good fit to the observations was achieved with the realistic parameters for the disk. These values are also summarized in Table 1.

Figures 4 and 5 depict both the observed spectra, as well as our synthetic fits for a few representative phases at both quadratures and during both eclipses to illustrate the most interesting effects. The observed spectra display red and blue emission features, as well as a central depression. The observed far wings of Hα stretching beyond the emission peaks in Figure 4 do not seem as deep as in the synthetic spectra. This is not a continuum rectification problem. These shallower observed wings were previously noted by Peters (1989) and interpreted as an emission stretching up to 30 Å from the line center. However, these observed far Hα wings in TT Hya differ from single-star standard spectra or from synthetic ones most probably because the atmospheric regions of the primary are more complicated. A number of additional effects could be expected here, such as a suction ("spray gun") effect of a disk moving over the atmosphere, centrifugal forces, and disk-atmosphere interaction with higher turbulence or temperatures. All of them tend to reduce the effective gravity of the atmosphere of the primary and the atmosphere-disk transition region. Note that the effective gravity is essentially zero in the disk. This could change the T-τ behavior of the atmosphere, mimic lower log g, reduce the pressure broadening, and, consequently, cause shallower line wings or shell spectra. It might be misleading to interpret these shallower wings as an emission (Peters 1989). The emission peaks and the central depression depend strongly on the phase, as best illustrated in Figure 6, for all observed and synthetic spectra. A discussion of the phase dependence of Hα, shown in Figures 4, 5, and 6, follows.

TABLE 1

Adopted Properties of TT Hya

Parameter	Value	Source
Primary		
M	2.63 $M_\odot$	VW
R	1.95 $R_\odot$	VW
log g	4.23	...
T	9800 K	VW, E
$v \sin i$	168 km s^{-1}	E
u	0.5	VW
a	22.63 $R_\odot$	VW
Secondary		
M	0.59 $M_\odot$	VW
log g	2.66	...
T_p	4600 K	BRM
u	0.8	VW
β	0.08	L
Disk		
i	82°.84	VW
α	2 $R_\odot$	BRM
$R_{\rm in}$	2 $R_\odot$	BRM
$R_{\rm out}$	10 $R_\odot$	BRM
$\rho(R_{\rm in})$	4×10^{-14} g cm^{-3}	BRM
$n_e(R_{\rm in})$	2×10^{10} cm^{-3}	BRM
T	6200 K	BRM
η	-1	BRM
$v_{\rm trb}$	30 km s^{-1}	BRM

Notes.—Designations: u = limb-darkening coefficient, a = separation of the components, T_p = temperature at the rotation pole, β = gravity-darkening exponent, i = inclination, α = vertical half-thickness, $R_{\rm in}$ = inner radius, $R_{\rm out}$ = outer radius, $\rho(R_{\rm in})$ = density, $n_e(R_{\rm in})$ = electron number density, η = exponent of the density power law, $v_{\rm trb}$ = microturbulence. Secondary was assumed to have synchronous rotation and to fill the Roche lobe.

References.—VW: Van Hamme & Wilson 1993; E: Etzel 1988; L: Lucy 1968; BRM: this work.

4.2.1. *First Quadrature*

The first quadrature (Fig. 4; phase 0.217) seems to have the simplest spectrum. Here we see a remarkably good agreement between the observed and theoretical profiles. Both emission peaks have approximately similar strength. A little bump on the red side of the central depression is the intrinsic Hα line of the secondary.

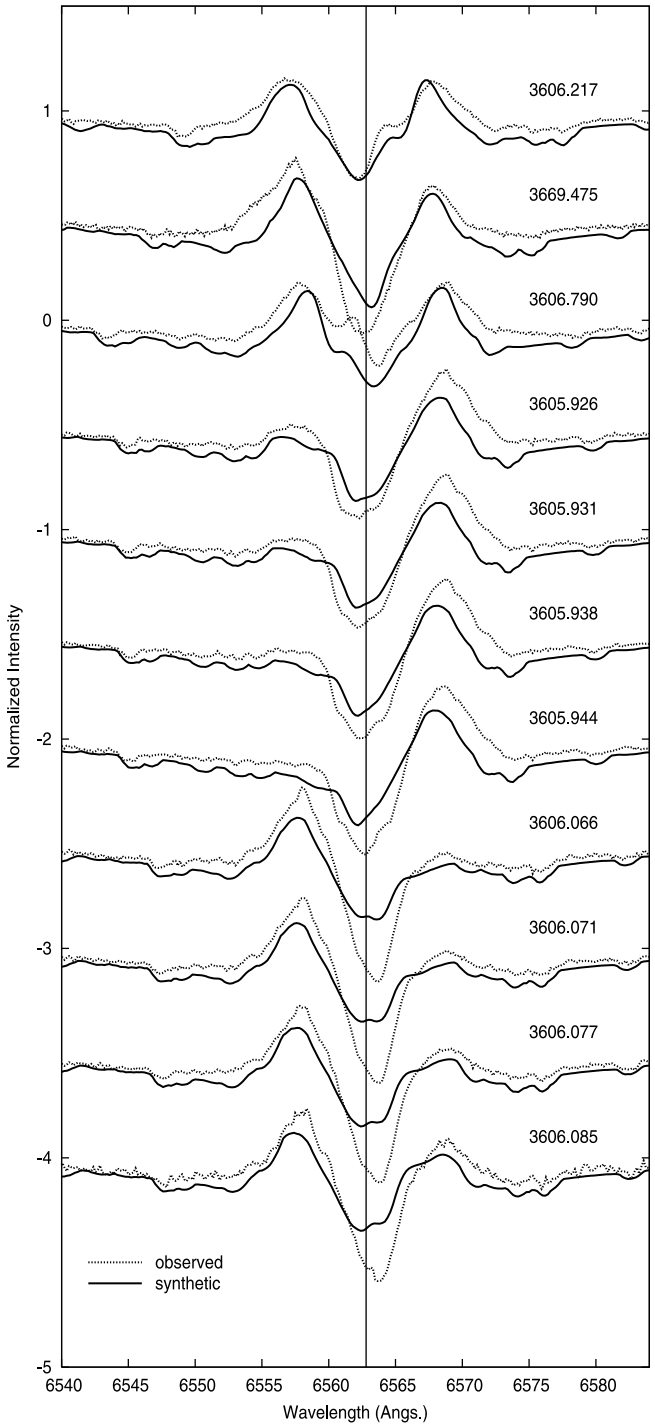

FIG. 4.—Synthetic spectra (*solid line*) compared with the observed Hα spectra (*dotted line*) of TT Hya at different phases. The vertical line indicates the laboratory wavelength. The systemic (gamma) velocity of the system (9.25 km s^{-1}) was subtracted from the observed spectra. The numbers to the right of the spectra indicate the epoch and phase of the observations.

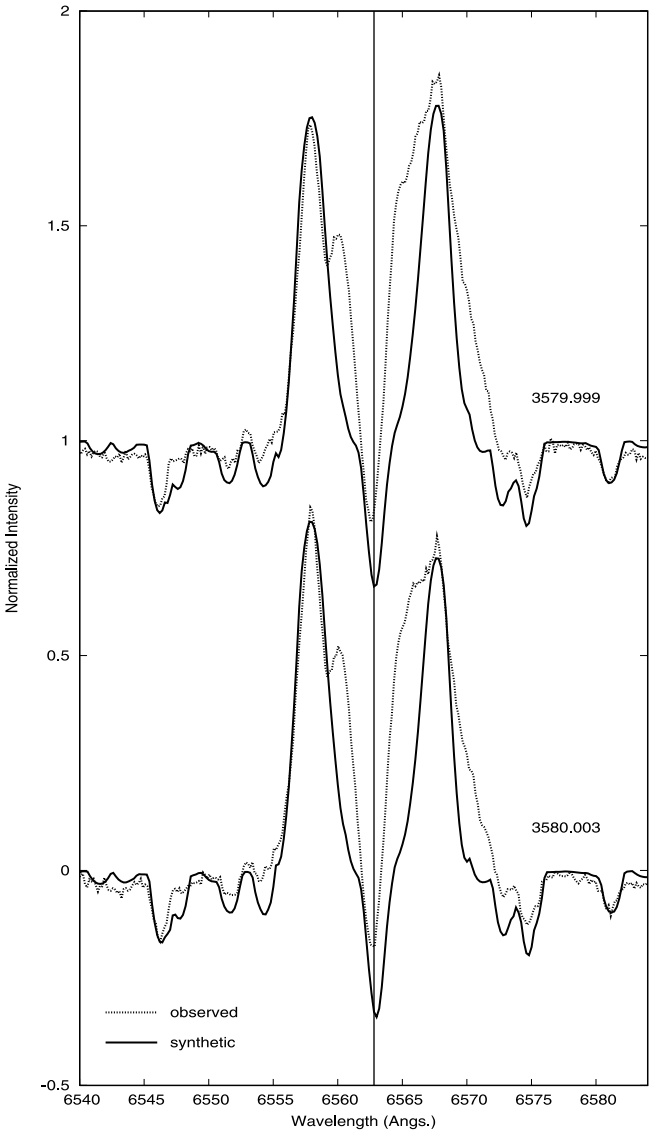

FIG. 5.—Synthetic (*solid line*) and observed (*dotted line*) Hα spectra of TT Hya during total eclipse. The numbers to the right of the spectra indicate the epoch and phase of the observations. The vertical line indicates the laboratory wavelength. The systemic (gamma) velocity of the system (9.25 km s^{-1}) was subtracted from the observed spectra.

4.2.2. *Secondary Eclipse*

As we proceed toward secondary eclipse, the blue emission gets apparently stronger than the red emission. This should not happen if the disk is symmetric and its source function does not depend on the phase. However, this effect is also observed in the synthetic spectra (see Figs. 6 and 4; phase 0.475) and is caused by the shadowing of the secondary by the disk. Just before secondary eclipse the receding parts (red emission) of the disk project onto the surface of the secondary. This imposes different boundary conditions for intensity, which is zero in the blue emission but nonzero in the red emission. An extra absorption of the secondary's light in the receding part of the disk causes the red emission to be reduced. This effect should be balanced in the middle of the eclipse, as seen in Figure 6. If this explanation is correct, the reverse (stronger red emission) should be observed after the middle of the eclipse at phases 0.5–0.6. Unfortunately, these phases are not well covered by the observations of B. Miller et al. (2005, in preparation), but Figure 4 of Peters (1989) confirms that this is really the case. At the same time during secondary eclipse both emission peaks grow slightly. This is mainly because the stellar continuum drops during the eclipse and the contribution of the emission to the total light can become more pronounced. This is also reproduced in the synthetic spectra, but the observed emission peaks are still stronger than the theoretical ones, which indicates that we may have underestimated the temperature of the secondary at this phase or overestimated the adopted limb darkening of the secondary. This might also be due to the reflection effect, which is not considered in our calculations.

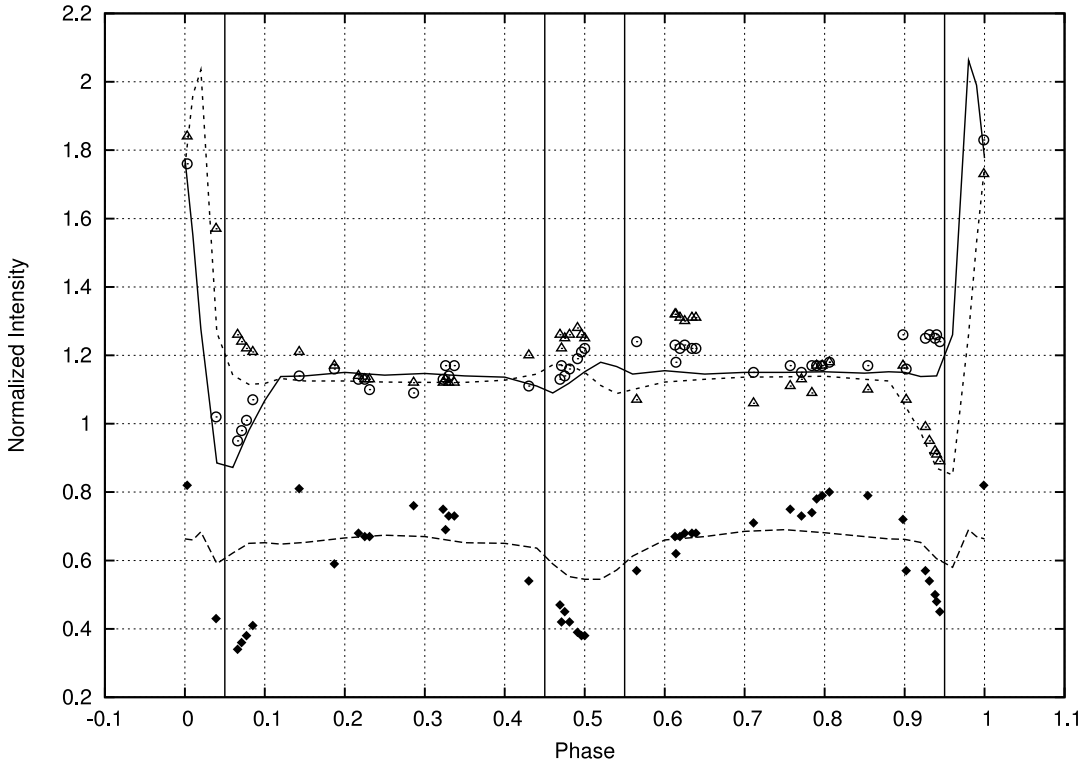

FIG. 6.—Behavior of the emission strength and central absorption depth of Hα during the orbit of TT Hya. Triangles show the highest normalized intensity of the blue emission peak; circles show the intensity of the red emission; diamonds show the depth of the central depression; long-dashed line shows the synthetic central depression; solid line shows synthetic red emission; short dashes show the synthetic blue emission. The vertical lines indicate the start and the end of primary and secondary (partial) eclipse. [*See the electronic edition of the Journal for a color version of this figure.*]

The blue emission extends to higher radial velocities (Fig. 4). This is not predicted by the synthetic spectra, and our interpretation is that this is evidence of the gas stream. At this phase in the blue emission we are looking through more inhomogeneous regions encompassing the gas stream and disk-stream interaction regions, which have higher than average radial velocity and can be rather turbulent, exhibiting the strongest departures from circular Keplerian velocities. This is probably also the reason why the observed central depression is displaced slightly to shorter wavelengths. The observed central depression gets very deep at these phases and reaches a minimum at about the middle of secondary eclipse. It is deeper than in the theoretical spectra. This huge depression could be caused by the combination of several effects: (1) at this phase the intrinsic Hα lines of both stars overlap, which deepens the central depression; (2) the reduction of the emission peaks by an additional absorption of light from the secondary by the disk might deepen the depression as well; (3) as pointed out above, if the surface of the secondary were hotter at this phase, it would make the intrinsic line of the secondary, as well as the overall central depression, deeper; and (4) the eclipse of the secondary lowers the stellar continuum and changes both emission and absorption.

Something unexpected happens after the eclipse during phases 0.6–0.7: the blue emission increases again. This does not seem to be a temporal effect, as can be seen in the earlier observations of Peters (1989; Fig. 4). One could expect to observe the reverse from the opposite line of sight within phases 0.1–0.2, but this is not the case. Could there exist some other circumstellar material apart from the disk and the stream in the system that contributes to the emission? If this source were projected onto the surface of the secondary at phases 0.6–0.7, it might have the same effect as the disk at phases 0.4–0.5 and might increase the relative strength of the blue emission. If this were the case, on symmetry grounds, we could expect the reverse (red emission stronger) at phases 0.3–0.4. There is only a very weak indication in Figure 6 that this might be the case. Independent data of Peters (1989) indicate the same effect, that the red emission is slightly stronger at phases 0.3–0.4. However, if this matter projects onto the secondary during 0.6–0.7 and 0.3–0.4, then it would have to be outside the Roche lobe of the primary. This will most likely be somewhere between the $C1$ and $C2$ Roche surfaces.

4.2.3. *Second Quadrature*

The emission at the other quadrature (Fig. 4; phase 0.790) looks similar to that at 0.217 and is well reproduced in the calculations, but now the observed central depression is weaker. The central absorption is smallest shortly after the quadrature at about 0.79–0.86 (Fig. 6). Our interpretation is that this is evidence of the hot spot or hotter disk regions projecting onto the stellar surface of the primary, which increases the source function along the line of sight and reduces the central depression. A little bump now seen on the blue side of the central depression is the intrinsic secondary Hα line.

4.2.4. *Eclipse of the Disk*

The next four phases depicted in Figure 4 (phases 0.926–0.944) represent the eclipse of the approaching part of the disk, and one can follow in both observed and theoretical spectra how the blue emission progressively ceases. The behavior of both emission peaks is thus explained fairly well with our model. Red emission seems to be stretching more to the red than predicted, but this is just the manifestation of the same effect observed close to the secondary eclipse for the blue emission. This time, before the primary eclipse in the red emission, we observe

the gas stream with higher receding velocities than expected from circular Keplerian orbits. However, the observed central absorption is again deeper than expected. Total eclipse, which follows, is discussed on a separate figure (Fig. 5) because of the different intensity scale.

The last four spectra in Figure 4 (phases 0.066–0.085) cover egress out of the disk eclipse. This time, one can observe how the red emission associated with the receding part of the disk emerges. Again, the behavior of the emission peaks is reproduced fairly well in the calculations; however, the observed central depression is much deeper than expected from our model and poses the most serious problem. To some extent it may be caused by the similar effect invoked for the explanation of the depression near secondary eclipse, i.e., overlap in radial velocities of stellar components (which operates only outside total eclipse this time). We also encounter the eclipse of the low-velocity emission regions that spill into the central absorption, which deepens the absorption. This is apparently not enough. There are several possible explanations for this additional absorption just before and after the primary eclipse. It can be ascribed (1) to the main body of the disk and assumed that the cooler disk regions project onto the hot surface of the primary slightly before but mainly after total eclipse. We reject this idea, since such cooler regions in the main body of the disk should manifest in asymmetric emission peaks at the quadratures, which are not observed. Another alternative is (2) to ascribe these deep Hα cores to the inner and more dense regions of the disk, as suggested by Peters (1989). This might have no significant effect on the emission peaks, but there is another problem with this interpretation, which is the strong phase dependence of this feature. There is no obvious reason why this absorption, if originating from inner disk regions, should be phase dependent. One could assume that an inner disk region close to a hot spot or a direct impact of the gas stream is hotter, but the matter would quickly cool toward the equilibrium value on timescales much shorter than a Keplerian period of the inner disk. Moreover, an enhanced absorption in the cores of Hα is observed only shortly before and after the primary eclipse and quickly changes and disappears within 0.1 orbital period between phases 0.85–0.95 and 0.05–0.15. Such an enhanced absorption is observed at the same phases in other Algols, e.g., β Per (Richards 1993), which does not have a permanent accretion disk. This leads us to suggest possibility (3), that this effect could be associated with some cooler matter in the vicinity of the secondary star or L2 point. One could speculate that it may have the form of a slightly asymmetric envelope or a "tail" accompanying the secondary during its orbital motion or perhaps circumstellar matter populating the region between the $C1$ and $C2$ critical Roche surfaces. In either situation, it is plausible that such matter could be present between $C1$ and $C2$ and could get there easily, since the secondary already fills the $C1$ surface and is a magnetically active star. The disk itself reaches almost up to the Roche lobe of the primary, and there is no reason to believe that it should have an abrupt end just before the Roche surface and not spill beyond the surface. The leading region (in the sense of the orbital movement) of such a secondary's envelope should be slightly hotter or less dense than the rear or tail of the envelope, since the excess absorption is deeper after primary eclipse.

There is still more to understand. Note that just before primary eclipse starts (0.90–0.95), the red emission is enhanced while the blue emission is being eclipsed. The opposite, even more pronounced effect is observed after the eclipse (0.05–0.10), when the red emission emerges out of eclipse as the blue emission gets fainter. It is not clear whether these features are permanent or transient or why the noneclipsed emission should be affected during the eclipse of the other emission. Possible explanations include (1) that the disk itself contributes significantly to the total continuum and this contribution is reduced during the disk eclipse or (2) the primary is being shadowed by the extra matter between $C1$ and $C2$ (as suggested above). We made a test calculation for phase 0.0 with and without the disk and found that the contribution of the uneclipsed disk to the whole light in the continuum at Hα at this phase was only about 5×10^{-4}. Thus, the second option would be more plausible. If the effect is real and the explanation correct, one could expect a drop in the R-band photometry light curve at the corresponding phases by about 0.05 mag.

4.2.5. *Total Eclipse*

Finally, Figure 5 exhibits the spectra during total eclipse. This is an important verification of the disk model, since at this phase the main source of light, the primary star, as well as the inner disk regions, is obscured. The spectral lines of the secondary star can be seen more clearly, and they indicate that the temperature of the secondary is probably slightly higher than the value of 4361 K found by Van Hamme & Wilson (1993). We adopted a temperature of 4600 K at the rotation pole of the secondary, which is reduced by about 200 K on the back side of the secondary because of gravity darkening. These phases also demonstrate that a slight decrease in the radial density profile of the disk is necessary to obtain better agreement with the observations. This radial density profile is described with the power-law behavior $\rho = \rho_{\rm in}(r/r_{\rm in})^{\eta}$ in our model, and the exponent $\eta = -1$ seems to fit the data best. Both emission peaks agree fairly well with the synthetic spectra. It is interesting that the red emission looks slightly wider than the blue emission. This is the manifestation of the same effect as described above at the phases just before primary eclipse or of the reversed effect seen close to secondary eclipse when the blue emission was wider because of the enhanced departures from a Keplerian velocity field due to the gas stream and stream-disk interaction. However, at total eclipse the main contribution seen is that from the remote part of the disk close to the Roche lobe and out of the disk plane. These areas may exhibit the strongest departures from our simple prescription of the Keplerian velocity (single star model), which might explain why the synthetic central depression is wider.

The calculated central depression during primary eclipse is slightly stronger than expected. This can be due to several reasons: First, the red emission, which is wider, overlaps the absorption and also skews it toward the blue. Second, the synthetic spectra were calculated for the temperature of 4600 K, which may be attained at the rotational pole, but the actual temperatures we observe at the back side of the secondary are lower by about 200 K and the intrinsic Balmer lines of the secondary would be noticeably weaker at such temperatures. Here we would like to point out that the skew of the central depression to the blue at these phases (close to the primary and secondary eclipse) can be easily misinterpreted as evidence of mass outflow. At the other phases, such as quadratures, departures from the circular Keplerian orbit may occur, causing a shift of the central absorption to either side. That is why we feel that such a blueshifted central depression is not proof of the mass outflow from the disk and that this conclusion of Peters (1989) should be revisited.

4.2.6. *Reliability of the Free Parameters of the Disk*

Since there are so many free parameters of the disk, we cannot claim that our fit is a unique solution. Nevertheless, as shown in the previous section, the parameters affect the spectrum in specific

ways that we now understand more clearly (see Figs. 1, 2, and 3). Consequently, such calculations can be used to put an independent constraint on many of these parameters. The calculations are not very sensitive to the inner radius of the disk, but they seem to indicate that it reaches the surface of the star; moreover, the density of the disk seems to increase toward the star. This is expressed by the negative exponent η. However, the exponent is best constrained from the emission strength during the total eclipse, which is also sensitive to the temperature of the secondary, and if the latter is wrong, a spurious value of η could be obtained. If we had adopted the cooler temperature of the secondary derived by Van Hamme & Wilson (1993), the effect would be to lower the continuum and make the emission peaks relatively stronger and the exponent η would have to be even more negative. The outer radius can be set much more reliably, since it strongly affects the separation of the emission peaks. The Roche lobe radius of the primary is about $10.6\,R_\odot$, so our value is realistic and is about 95% of the Roche lobe. This is in perfect agreement with the value suggested by Peters (1989), who estimated that the disk spans 95% of the Roche lobe. The exact agreement is a coincidence, since in practice the disk probably does not have an abrupt end but rather dissolves smoothly.

The vertical dimension of the disk is significant and is of the order of the dimension of the primary star. It agrees with the estimates of Peters (1989) and Plavec (1988), since it is in the region where both their estimates overlap. The temperature of the disk that we obtained should be viewed as a characteristic temperature of the Hα-emitting regions. In reality, there may be strong local departures from such a homogeneous model. Regions with temperatures between 5000 and 30,000 K will contribute significantly to the Balmer line emission, but both cooler and hotter regions may manifest at different wavelengths or spectral lines and an image of the disk can change depending on the spectral feature studied. The temperature was inferred mainly from the central depression, which is strongly variable, and there may be other effects that are beyond the scope of the paper and may turn out to be important, such as NLTE effects, a better treatment of the line absorption coefficient, and scattering at optically thick wavelengths.

The densities are quite well determined, since the overall emission is very sensitive to this parameter. Nevertheless, in reality, again strong local departures can be expected from such a simple density profile. The densities we obtained throughout the disk decline from $n_e = 2 \times 10^{10}$ cm^{-3} at the inner radius to $n_e = 4 \times 10^{9}$ cm^{-3} at the outer radius. They are in very good agreement with the estimate of Peters (10^{10} cm^{-3}; 1989). The assumed microturbulence is very uncertain. In the case of an optically thin disk, it should be viewed as a departure from the Keplerian velocity field rather than a local turbulence, and we can claim only that these departures will not be higher than about 80 km s^{-1}. However, these departures may be higher in the gas stream. Consequently, we can claim that the single-star disk model with a Keplerian velocity field (as given by eq. [43]) can reproduce the shape of the line fairly well. The regions of the disk out of the orbital plane and close to the Roche lobe are most vulnerable to departures from this model.

The Voigt profile is generally not a good approximation for hydrogen lines; however, it can be justified in the case of emission lines originating from low-density regions where the line profile is determined mainly by the three-dimensional velocity field. Finally, we would like to point out that the parallax measured by *Hipparcos* corresponds to a distance of about 154 ± 25 pc, which is not in very good agreement with the previous estimates of Etzel (1988) and Plavec (1988), who both obtained distances of about 194 pc. If the new distance is confirmed by future parallax measurements, then either the geometrical scale (semimajor axis) and stellar radii are smaller than those obtained by Etzel (1988), Plavec (1988), or Van Hamme & Wilson (1993) or the temperatures of the stars, mainly that of the primary, might have to be reduced slightly.

5. SUMMARY AND CONCLUSIONS

We have developed a new computer code called SHELLSPEC. This is to our knowledge the only tool that can produce the synthetic light curves and synthetic spectra of interacting binaries taking into account optically thin moving circumstellar matter. The code was applied to the well-known eclipsing Algol-type binary system TT Hya, which has an accretion disk. Synthetic spectra of the system for all phases were calculated by taking into account a spherical primary and a Roche lobe–filling secondary, as well as a disk. For the first time, it has been verified by calculations of synthetic spectra that the double-peaked emission in TT Hya, and thus also in other long-period Algol-type eclipsing binaries, originates from circumstellar matter in the form of an accretion disk with a Keplerian velocity field.

The effect on the spectrum of various free parameters was studied. The temperature and inclination of the disk have the strongest effect on the depth of the central depression, while the outer radius of the disk, the radial density profile, and the inclination affect mainly the position and separation of the emission peaks. The overall strength of the emission is regulated mainly by the density and temperature. The central depression was found to be created by two different effects: the geometry and the velocity field of the disk itself and the cool matter projected onto the hotter stellar surface.

Realistic estimates of the densities, temperature, geometry, and dynamics of the disk were obtained as a result of these calculations. However, there are differences between the observed and synthetic spectra, which assume a simple circular Keplerian disk. These can be attributed mainly to the gas stream or stream-disk interaction. The presence of an additional source of circumstellar matter in the system between the $C1$ and $C2$ Roche surfaces is suggested to account for the deep absorption in the Hα cores detected near primary eclipse and various other observed features.

We would like to thank Ivan Hubeny, Alon Retter, and the referee for their comments and suggestions and Pavel Koubský for kindly allowing us to use our jointly collected 1996/1997 spectra of TT Hya prior to publication. J. B. gratefully acknowledges grant support from Penn State University and thanks Konstatin Getman, and department computer staff for their assistance with computer-related problems. This research was supported by the NSF-NATO Fellowship (NSF DGE-0312144) and partly by VEGA grant 3014 from the Slovak Academy of Sciences and the Science and Technology Assistance agency under contract 51-000802.

REFERENCES

Albright, G. E., & Richards, M. T. 1996, ApJ, 459, L99
Bradstreet, D. H., & Steelman, D. P. 2002, BAAS, 34, 1224
Budaj, J., & Dworetsky, M. M. 2002, MNRAS, 337, 1340
Budaj, J., Dworetsky, M. M., & Smalley, B. 2002, Commun. Univ. London Obs. 82, http://www.ulo.ucl.ac.uk/ulo_comms/82/index.html
Budaj, J., & Richards, M. T. 2004, Contrib. Astron. Obs. Skalnaté Pleso, 34, 167

Cherepashchuk, A. M., Eaton, J. A., & Khaliullin, K. F. 1984, ApJ, 281, 774
Claret, A. 1998, A&AS, 131, 395
Djurasevic, G. 1992, Ap&SS, 197, 17
Drechsel, H., Haas, S., Lorenz, R., & Mayer, P. 1994, A&A, 284, 853
Eaton, J. A., & Henry, G. W. 1992, Inf. Bull. Variable Stars, 3737
Etzel, P. B. 1988, AJ, 95, 1204
Grevesse, N., & Sauval, A. J. 1998, Space Sci. Rev., 85, 161
Hadrava, P. 1997, A&AS, 122, 581
Hilditch, R. W. 2001, An Introduction to Close Binary Stars (Cambridge: Cambridge Univ. Press)
Hill, G. 1979, Publ. Dom. Astrophys. Obs. Victoria, 15, 297
Horne, K., & Marsh, T. R. 1986, MNRAS, 218, 761
Hubeny, I. 1988, Comput. Phys. Commun., 52, 103
Hubeny, I., & Lanz, T. 1992, A&A, 262, 501
———. 1995, ApJ, 439, 875
Hubeny, I., Lanz, T., & Jeffery, C. S. 1994, in Newsletter on Analysis of Astronomical Spectra 20, ed. C. S. Jeffery (CCP7; St. Andrews: St. Andrews Univ.), 30
Karetnikov, V. G., Menchenkova, E. V., & Nazarenko, V. V. 1995, Astron. Nachr., 316, 163
Kopal, Z. 1959, Close Binary Systems (London: Chapman & Hall)
Krtička, J. 1998, in Proc. 20th Stellar Conf., ed. J. Dušek & M. Zejda (Brno: Nicholas Copernicus Obs. Planetarium), 73
Krtička, J., & Kubát, J. 2002, A&A, 388, 531
Kubát, J. 2001, A&A, 366, 210
Kulkarni, A. G., & Abhyankar, K. D. 1980, Ap&SS, 67, 205
Kurucz, R. L. 1993a, Kurucz CD-ROM 18, SYNTHE Spectrum Synthesis Programs and Line Data (Cambridge: SAO)
———. 1993b, Kurucz CD-ROM 13, ATLAS9 Stellar Atmosphere Programs and 2km/s grid (Cambridge: SAO)
la Dous, C. 1989, A&A, 211, 131
Limber, D. N. 1963, ApJ, 138, 1112
Linnell, A. P., & Hubeny, I. 1996, ApJ, 471, 958
Long, K. S., & Knigge, C. 2002, ApJ, 579, 725
Lucy, L. B. 1968, ApJ, 153, 877
Mochnacki, S. W., & Doughty, N. A. 1972, MNRAS, 156, 51
Orosz, J. A., & Wade, R. A. 2003, ApJ, 593, 1032
Perryman, M. A. C., et al. 1997, The *Hipparcos* and Tycho Catalogues (ESA SP-1200; Noordwijk: ESA)
Peters, G. J. 1989, Space Sci. Rev., 50, 9
Peters, G. J., & Polidan, R. S. 1998, ApJ, 500, L17
Piskunov, N. E. 1992, in Stellar Magnetism, ed. Yu. V. Glagolevskij & I. I. Romanyuk (Saint Petersburg: Nauka), 92
Plavec, M. J. 1988, AJ, 96, 755
Plavec, M. J., & Kratochvil, P. 1964, Bull. Astron. Inst. Czechoslovakia, 15, 165
Plavec, M. J., & Polidan, R. S. 1976, in IAU Symp. 73, Structure and Evolution of Close Binary Systems, ed. P. Eggleton, S. Mitton, & J. Whelan (Dordrecht: Reidel), 289
Popper, D. M. 1989, ApJS, 71, 595
Press, W. H., Flannery, B. P., Teukolsky, S. A., & Vetterling, W. T. 1986, Numerical Recipes (Cambridge: Cambridge Univ. Press)
Pribulla, T. 2004, in ASP Conf. Ser. 318, Spectroscopically and Spatially Resolving the Components of Close Binary Stars, ed. R. Hilditch et al. (San Francisco: ASP), 117
Proga, D., Kallman, T. R., Drew, J. E., & Hartley, L. E. 2002, ApJ, 572, 382
Richards, M. T. 1993, ApJS, 86, 255
Richards, M. T., & Albright, G. E. 1999, ApJS, 123, 537
Richards, M. T., & Ratliff, M. A. 1998, ApJ, 493, 326
Rucinski, S. W. 1973, Acta Astron., 23, 79
Rybicki, G. B., & Hummer, D. G. 1983, ApJ, 274, 380
Sahade, J., & Cesco, C. U. 1946, ApJ, 103, 71
Smith, K. C. 1992, Ph.D. thesis, Univ. London
Smith, K. C., & Dworetsky, M. M. 1988, in Elemental Abundance Analyses, ed. S. J. Adelman & T. Lanz (Lausanne: Inst. Astron. Univ. Lausanne), 32
Van Hamme, W., & Wilson, R. E. 1993, MNRAS, 262, 220
Vinkó, J., Hegedüs, T., & Hendry, D. 1996, MNRAS, 280, 489
Wade, R. A., & Hubeny, I. 1998, ApJ, 509, 350
Wilson, R. E., & Devinney, E. J. 1971, ApJ, 166, 605
Zhang, E.-H., Robinson, E. L., & Nather, R. E. 1986, ApJ, 305, 740